Article

Influence of $Bi_{1.5}Y_{0.5}O_3$ Active Layer on the Performance of Nanostructured $La_{0.8}Sr_{0.2}MnO_3$ Cathode

Javier Zamudio-García [1,*], Nerea Albarrán-Aroca [2], José M. Porras-Vázquez [1], Enrique R. Losilla [1] and David Marrero-López [2,*]

[1] Deparment of Inorganic Chemistry, University of Málaga, 29071 Málaga, Spain; josema@uma.es (J.M.P.-V.); r_losilla@uma.es (E.R.L.)

[2] Department of Applied Physics I, University of Málaga, 29071 Málaga, Spain; nereaalbarranaroca@gmail.com

* Correspondence: zamudio@uma.es (J.Z.-G.); marrero@uma.es (D.M.-L.); Tel.: +34-9521-37057 (J.Z.-G.); +34-9521-37057 (D.M.-L.)

check for updates

Abstract: The efficiency of solid oxide fuel cell cathodes can be improved by microstructural optimization and using active layers, such as doped bismuth oxides. In this work, $Bi_{1.5}Y_{0.5}O_3$ (BYO) films are prepared by spray-pyrolysis deposition at reduced temperatures on a $Zr_{0.84}Y_{0.16}O_{1.92}$ (YSZ) electrolyte. The influence of the BYO film on the performance of an $La_{0.8}Sr_{0.2}MnO_3$ (LSM) cathode prepared by traditional screen-printing and spray-pyrolysis is investigated. A complete structural, morphological, and electrochemical characterization is carried out by X-ray diffraction, electron microscopy, and impedance spectroscopy. The incorporation of BYO films decreases the Area Specific Resistance (ASR) of screen-printed cathodes from 6.4 to 2.2 Ω cm^2 at 650 °C. However, further improvements are observed for the nanostructured electrodes prepared by spray-pyrolysis with ASRs of 0.55 and 1.15 Ω cm^2 at 650 °C for cathodes with and without an active layer, respectively. These results demonstrate that microstructural control using optimized fabrication methods is desirable to obtain high-efficiency electrodes for solid oxide fuel cell (SOFC) applications.

Keywords: $La_{0.8}Sr_{0.2}MnO_3$; $Bi_{1.5}Y_{0.5}O_3$; solid oxide fuel cell; spray-pyrolysis; active layer

1. Introduction

Solid oxide fuel cells (SOFCs) are considered a highly promising technology for clean and efficient power generation [1,2]. However, several issues should be addressed, such as the reduction in the current operating temperature to an intermediate range of 500–750 °C to promote their development and commercialization. In particular, the cell efficiency at low temperatures is mainly limited by the oxygen reduction reaction (ORR) in the cathode [3].

$La_{1-x}Sr_xMnO_3$ (LSM) is still the most widely used cathode material due to its high chemical and thermal stability under the severe operating conditions of the cell, as well as excellent compatibility with the common electrolyte material, yttria stabilized zirconia (YSZ) [4,5]. However, LSM exhibits a poor ionic conductivity and relatively high activation energy for the oxygen reduction reaction, reducing drastically its electrochemical performance at intermediate temperatures [6,7]. Different strategies have been explored to overcome this limitation: (i) combining LSM with ionic conducting materials, such as YSZ, doped-CeO_2, and Bi_2O_3-based electrolytes [8–10]; (ii) the preparation of nanostructured LSM cathodes with an extended triple-phase boundary (TPB) for the oxygen reduction reaction [7,11]; and (iii) the introduction of an active interlayer with a high ionic conductivity to enhance the oxide ion transfer from the cathode to the electrolyte [12,13].

Bismuth oxide stabilized with Er^{3+} or Y^{3+} has showed to be an effective active layer due to its superior oxide ion conductivity compared to YSZ and doped-CeO_2 [14,15]. These active layers are traditionally prepared by screen-printing [16,17] and dip-coating [18,19] at high sintering temperatures for long times to achieve both dense films and a good adhesion to the electrolyte. However, Bi evaporates at a relatively low temperature, and therefore low-temperature fabrication methods are needed. Physical deposition methods, such as pulsed laser deposition [20,21] and magnetron-sputtering [14,22], have been also employed; nevertheless, these methods are not economic for industrial implementation. In this context, spray-pyrolysis has shown to be an effective method for the preparation of different materials for SOFCs, including electrolytes, electrodes, and barrier layers [23,24]. This method has several advantages, including the preparation of material layers in a single deposition/sintering step, its low cost, its shorter preparation time, and its easy implementation at industrial scale as a continuous process over large surfaces. Moreover, the sintering temperature is significantly reduced, minimizing the chemical reactivity between the cell components.

In this work, nanostructured LSM cathodes with and without $Bi_{1.5}Y_{0.5}O_3$ (BYO) active layers are obtained by spray-pyrolysis deposition. The structure and morphology of the layers are studied by X-ray diffraction and scanning electron microscopy, respectively. An exhaustive electrochemical characterization by impedance spectroscopy is carried out at different temperatures and oxygen partial pressures to determine the different processes involved in the ORR, as well as the effect of the BYO layer on the efficiency of LSM cathodes. The results are compared with those obtained for traditional cathodes fabricated by the screen-printing method.

2. Materials and Methods

$Zr_{0.84}Y_{0.16}O_{1.92}$ (YSZ) pellets were prepared from commercial powders supplied by Tosoh. These were compacted into disks of 10 and 1 mm diameter and thickness, respectively, and then sintered in air at 1400 °C for 4 h to obtain fully dense electrolytes.

For the preparation of the $Bi_{1.5}Y_{0.5}O_3$ (BYO) layers by spray-pyrolysis, stoichiometric amounts of $Bi(NO_3)_3 \cdot 6H_2O$ and $Y(NO_3)_3 \cdot 6H_2O$ (Merck, purity above 99%) were dissolved in Milli-Q water under continuous stirring to form a yellow transparent solution with a cation concentration of 0.01 mol L^{-1}. Citric acid was used as a complexing agent in a relation of ligand:metal of 0.5:1 to prevent phase segregations. Films prepared without citric acid were a mixture of monoclinic and cubic polymorphs of Bi_2O_3. The spray-pyrolysis setup and deposition conditions were similar to those described previously for related materials [11]. Briefly, the YSZ substrates were previously heated at 450 °C, and then the precursor solution was atomized and sprayed onto both pellet faces for 15 min with a flow rate of 20 mL h^{-1}. After that, the films were calcined between 600 and 800 °C for 1 h in a furnace to achieve crystallization.

The $La_{0.8}Sr_{0.2}MnO_3$ (LSM) cathode was deposited by spray-pyrolysis onto YSZ substrates with and without BYO interlayers from an aqueous precursor solution (0.02 mol L^{-1}), containing stoichiometric amounts of $La(NO_3)_3 \cdot 6H_2O$, $Sr(NO_3)_2$, and $Mn(NO_3)_2 \cdot 4H_2O$ (Merck, purity above 99%). This precursor solution was sprayed onto the YSZ and YSZ/BYO substrates, preheated at 250 °C, for 1 h with a flow rate of 20 mL h^{-1} [7]. Finally, the samples were calcined in a furnace to completely decompose the precursors and crystallize the cathodes at 800 °C for 1 h. Hereafter, the samples prepared by spray-pyrolysis are labelled with SP.

For comparison purposes, commercial $La_{0.8}Sr_{0.2}MnO_{3-\delta}$ (LSM) powders supplied by Praxair[®] were mixed with Decoflux binder to obtain an ink, which was screen-printed onto the as-prepared YSZ substrates and BYO active layers, followed by sintering at 1000 °C for 1 h to ensure sufficient adherence.

Structural, Microstructural, and Electrical Characterization

The phase composition and structure were studied by X-ray powder diffraction (XRD) with an Empyrean PANalytical diffractometer and $CuK_{\alpha 1,2}$ radiation. The different phases were identified and analyzed with the Highscore Plus and GSAS suite software [25,26].
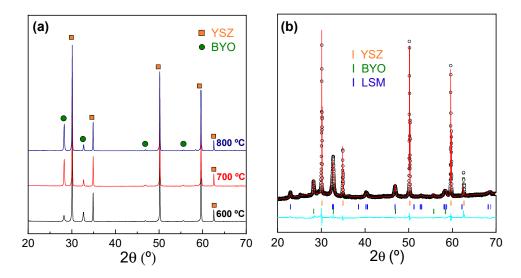
The morphology and elemental analysis of the different samples were analyzed by field emission scanning electron microscopy in a FEI-SEM (Helios Nanolab 650) coupled with X-ray dispersive spectroscopy (EDS, X-Max Oxford instrument, High Wycombe, UK).

The impedance spectra of the symmetrical cells were collected with a Solartron 1260. The frequency range and the AC amplitude applied were $0.01–10^6$ Hz and 100 mV, respectively. Pt-ink (METALOR® 6082) was painted on both faces of the pellets and then heated at 750 °C for 30 min to obtain a current collector layer. Furthermore, the impedance spectra were collected as a function of the oxygen partial pressure ($10^{-3}–1$ atm) at 650 °C to study the different processes involved in the ORR. The data were simulated by equivalent circuit models and the distribution of relaxation times (DRT) with the help of the ZView and DRTtools software, respectively [27,28].

3. Results and Discussion

3.1. Structural and Microstructural Analysis

The XRD patterns of BYO films prepared by spray-pyrolysis onto YSZ substrates at 450 °C for 15 min and then calcined at different temperatures are compared in Figure 1a. The different reflections are assigned to the YSZ substrate and the BYO film, both with a cubic fluorite-type structure. The BYO film shows a higher crystallinity as the temperature increases, and more importantly no additional peaks attributed to secondary phases are detected up to 800 °C. In addition, no appreciable shift of the diffraction peaks is observed, indicating that the cell volume and structure are not affected by the thermal treatment. The estimated average crystal size of BYO, calculated by the Scherrer equation after correction for instrumental broadening, increases from 26 nm at 600 °C to 47 nm at 800 °C. These values are relatively low in comparison with those obtained by conventional preparation methods, such as screen-printing (e.g., 500 nm for films deposited at 800 °C for 2 h [14]), due to the shorter sintering time and low temperature used in this work, which inhibit the grain growth.
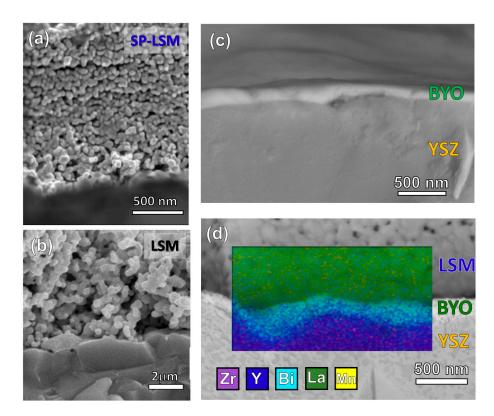

Figure 1. X-ray diffraction patterns of (**a**) $Bi_{1.5}Y_{0.5}O_3$ (BYO) films deposited on $Zr_{0.84}Y_{0.16}O_{1.92}$ (YSZ) substrates after calcining at different temperatures, and (**b**) Rietveld analysis of $La_{0.8}Sr_{0.2}MnO_3$ cathode deposited on BYO layer (SP-BYO/LSM).

Figure 1b shows the XRD Rietveld analysis of the LSM cathode deposited by spray-pyrolysis on the BYO/YSZ substrate after calcining at 800 °C. Three different crystalline phases, assigned to the YSZ electrolyte, the BYO active layer, and the LSM cathode, are observed without the presence of secondary phases. The Rietveld analysis is performed by considering two cubic fluorite-type phases (s.g. Fm-3m) for both YSZ and BYO and a rhombohedral structure (s.g. R-3c) for LSM, obtaining a successful disagreement factor: Rwp = 5.15% (Figure 1b). The unit cell volumes for BYO and LSM are

164.275(2) and 350.357(1) Å3, respectively, in good agreement with those reported in the literature for the bulk materials [7,29].

Cross-sectional SEM images of the symmetrical cells are displayed in Figure 2. The LSM cathode prepared by spray-pyrolysis at 800 °C has a particle size of ~50 nm and is highly porous, ensuring effective gas diffusion inside the cathode (Figure 2a). In contrast, the LSM cathode prepared by the screen-printing method shows a large particle size of 500 nm due to the higher sintering temperature required to obtain a good adhesion to the electrolyte (Figure 2b).

Figure 2. SEM image of (**a**) LSM cathode prepared by spray-pyrolysis; (**b**) LSM cathode prepared by screen-printing; (**c**) backscattering SEM, showing the dense BYO film deposited on the YSZ electrolyte; and (**d**) EDS mapping analysis of the different layers of the cells.

A backscattering SEM image reveals that the BYO films are dense with a thickness of ~200 nm and a good adhesion to the electrolyte (Figure 2c). Furthermore, the BYO film covers uniformly the electrolyte surface without the presence of delaminations or cracks, confirming that spray-pyrolysis deposition is a useful method for the preparation of BYO films at low temperatures. EDS analysis after LSM deposition shows clearly the elemental distribution of the different layers without appreciable cation interdiffusion between the cell components (Figure 2d). Furthermore, the theoretical and experimental cation compositions of the different layers are similar (Supplementary Information Tables S1–S3).

3.2. Electrochemical Properties

Figure 3a–c show the impedance spectra for the different symmetrical cells prepared by spray-pyrolysis deposition on YSZ substrates without and with a BYO active layer. For comparison purposes, Figure 3d–f show the spectra for the same symmetrical cell with LSM deposited by the traditional screen-printing method. Note that the ohmic resistances were subtracted for a better comparison of the electrode contribution. All the spectra were fitted using the equivalent circuits given in Figure 3g–i, where *L* is an inductor attributed to the electrochemical setup and R_E is a serial resistance related with the total ohmic resistance of the electrolyte. Two serial (*RQ*) elements, where *R* is the resistance in parallel with a constant phase element *Q*, are included to model the electrode

response at high frequency and low frequency, HF and LF, respectively. The high-frequency process is typically associated with charge transfer at the electrolyte/electrode interface, while the low frequency contribution is assigned to the absorption/dissociation of oxygen molecules at the LSM cathode surface [7]. In the low temperature range ($T < 450\,°C$), the bulk (B) and grain boundary contributions (GB) of the electrolyte are discernible, and the equivalent circuit of Figure 3i was considered.
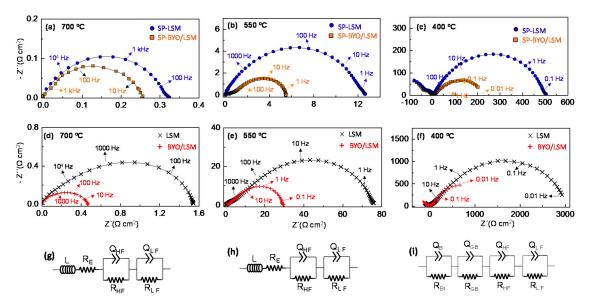

Figure 3. Impedance spectra of LSM and BYO/LSM symmetrical cells with LSM prepared by (**a–c**) spray-pyrolysis and (**d–f**) screen-printing at different measuring temperatures. (**g–i**) Equivalent circuits used to fit the data. The solid lines in the spectra represent the fitting curve with the proposed equivalent circuits.
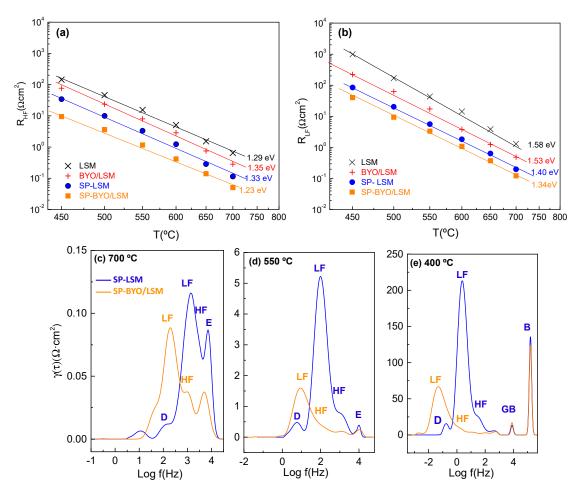
The following parameters were obtained for each electrode contribution: resistance R_i, pseudocapacitance Q_i, and the exponential parameter n_i. These parameters are related to the true capacitance C_i and relaxation frequency f_i by the following equations [23]:

$$C_i = \frac{(R_i Q_i)^{1/n_i}}{R} \tag{1}$$

$$f_i = \frac{1}{2\pi R_i C_i} \tag{2}$$

The representative fitting parameters obtained by equivalent circuits are given in Table S4.

The impedance spectra confirm that the total electrode polarization resistance is lower for all cells containing the BYO active layer. A detailed analysis of the data reveals that the high-frequency process decreases significantly after the introduction of the BYO interlayer due to the improved oxide ion transfer at the electrolyte/interface (Figure 4a). A similar behavior was reported for other active layers—e.g., $Ce_{0.1}Gd_{0.1}O_{1.95}$, $Ce_{0.9}Pr_{0.1}O_{1.95}$, and $SrFeO_3$ [12,30–33]. The corresponding activation energy varies between 1.23 and 1.35 eV.

Figure 4. Variation of the (**a**) high- and (**b**) low-frequency resistance contributions for the different cathode configurations; (**c**–**e**) Distribution of relaxation time (DRT) analysis at different temperatures.

In the case of the LF process, a similar behavior is observed, where the resistance decreases with the introduction of the BYO layer (Figure 4b). This indicates that the BYO layer not only improves the charge transfer due to better oxide-ionic conduction at the interface, but also promotes the extension of the surface path of the electrochemical reaction sites to the active interlayer. Furthermore, the activation energy of the LF process is higher than that of the HF process, and varies in a broad range from 1.58 eV for LSM to 1.34 eV for SP-LSM/BYO.

The DRT analysis confirms that the cathode response is formed by two main electrode contributions, attributed to the oxide ion transfer between the cathode/electrolyte interface and the oxygen surface exchange process at a high (HF) and low (LF) frequency, respectively (Figure 4c–e) [34]. In addition, a small process due to gas diffusion limitations into the electrode, labelled as D, has been identified at a low frequency [35]. It has to be noted that the integral area under each peak is equivalent to the polarization resistance of the corresponding process [36].
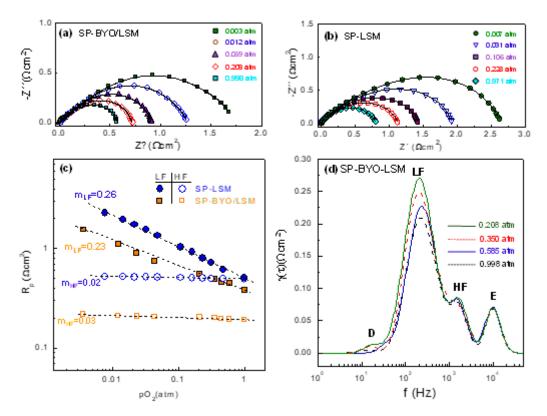
It is also observed that the introduction of the BYO active layer involves a displacement of the electrode contribution to lower frequencies, attributed to the fast oxide ion conductivity of the bismuth oxide layers [37,38]. The LF process is the main contribution in the whole temperature range, although it decreases significantly at high temperatures due to the higher activation energy of the oxygen exchange process. The process centered at 10^4 Hz is assigned to the ohmic resistance of the electrolyte (E) (Figure 4c,d). In the low temperature range ($T \leq 400\,°C$), the two contributions located at 10^4 and 10^5 Hz correspond to the bulk (B) and grain boundary (GB) contributions of the electrolyte, respectively (Figure 4e) [39]. As expected, the electrolyte contributions are not affected by the presence of the BYO layer, and they appear at the same frequency for cathodes with and without an active layer. The shift of

the electrode processes to lower frequencies after the BYO introduction is consistent with the equivalent circuit analysis, where the capacitances of the HF and LF processes increase in two orders of magnitude in cathodes containing the active layers. This increase in capacitance is usually related to an increase in active sites for the ORR; a similar behavior has been observed for nanostructured electrodes [7].

In order to obtain further insights into the rate-limiting-steps involved in the ORR, the impedance spectra were acquired as a function of the oxygen partial pressure (pO_2). Figure 5a,b display the variation of the impedance spectra of SP-LSM and SP-BYO/LSM. As expected, the polarization resistance increases at low oxygen partial pressure, but the number of processes remains unchanged. Hence, the equivalent circuit proposed above (Figure 3g–i) is used to fit the data in the whole pO_2 range. The resistance of the different processes, which involves surface adsorption/dissociation, gas diffusion, or charge transfer reactions are pO_2-dependent, according to the following expression [3,33]:
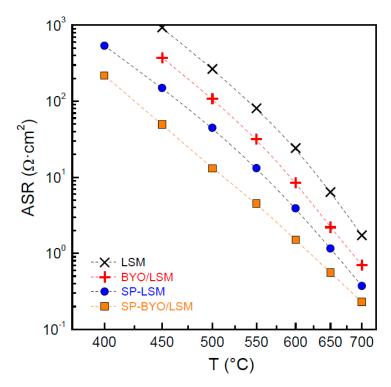
$$R_i \propto (pO_2)^{-m} \tag{3}$$

where *m* provides information about the type of process involved in the oxygen reduction reactions. Figure 5c compares the variation in the HF and LF resistance contributions as a function of pO_2. This figure clearly indicates that the low-frequency contribution is the main rate-limiting step for the ORR, especially at low pO_2. For both samples, the HF contribution is nearly pO_2-independent with a slope of $m\sim0.02$–0.03, suggesting that molecular or atomic oxygen are not involved in this process and, therefore, may be assigned to the O^{2-} transfer at the YSZ/LSM interface. In contrast, the LF contribution with $m\sim0.25$ is attributed to the charge-transfer reaction on the electrode surface [33].

Figure 5. Impedance spectra of (**a**) SP-BYO/LSM; (**b**) SP-LSM at 650 °C and different pO_2; (**c**) dependence of the cathode resistance contributions on pO_2; and (**d**) the DRT analysis of SP-BYO/LSM.

The DRT analysis of the impedance spectra confirms that the electrolyte contribution (E) and the HF process of the electrode polarization are pO_2-independent as expected; however, the LF process is affected by changes in the oxygen concentration (Figure 5d). At low pO_2 values, a new process (D) appears at ~10 Hz, which could be assigned to gas diffusion limitations, as observed previously [35].

Figure 6 compares the area specific resistance (ASR) of the different cathodes. The highest ASR values are found for the blank LSM cathode prepared by the traditional screen printing method—i.e., 6.4 Ω cm^2 at 650 °C. The introduction of a BYO active layer leads to a significant ASR decrease up to ~2.2 Ω cm^2. However, nanostructured LSM cathodes prepared by spray-pyrolysis exhibit lower ASR values than those of the corresponding screen-printed cathodes—i.e., 1.15 and 0.55 Ω cm^2 at 650 °C for SP-LSM and SP-BYO/LSM, respectively. This behavior is explained by the higher TPB length of the nanostructured LSM cathodes, as well as the lowest fabrication temperature, which minimize the reactivity between the cell layers. These results demonstrate that active layers could be used to improve the performance of SOFC cathodes; however, the optimization of the electrode microstructure leads to better electrochemical properties.

Figure 6. Area specific resistance (ASR) values of the different LSM cathodes as a function of the temperature.

4. Conclusions

The influence of BYO active layer on the performance of micrometric and nanostructured LSM cathodes prepared by screen-printing and spray-pyrolysis deposition, respectively, was investigated.

Dense and thin BYO films were successfully prepared on YSZ electrolyte at a reduced temperature to avoid possible Bi loss by evaporation. The LSM cathode prepared by spray-pyrolysis deposition showed an average particle size of 50 nm compared to 500 nm for the screen-printing cathode, which leads to the extended triple-phase length for the ORR.

The analysis of the impedance spectra confirmed the presence of two dominant electrode processes for cathodes with and without BYO active layers, which were assigned to O^{2-} transfer at the LSM/YSZ interface and the charge transfer reaction at the electrode surface. The introduction of a BYO layer decreased the resistances of both the high- and low-frequency contributions, suggesting that the active layer not only improves the charge transfer at the electrolyte interface but also extends the surface path of the electrochemical reaction sites.

The total polarization resistance for the different cathode configurations decreased in the order: LSM < LSM/BYO < SP-LSM < SP-BYO/LSM, indicating that the performance is further improved by increasing the electrode surface and TPB sites rather than the introduction of an active interlayer. Thus,

the microstructural optimization is the most recommendable method to improve the efficiency of the SOFC cathodes and reduce the operating temperature of these electrochemical devices.

References

1. Kan, W.H.; Samson, A.J.; Thangadurai, V. Trends in electrode development for next generation solid oxide fuel cells. *J. Mater. Chem. A* **2016**, *4*, 17913–17932. [CrossRef]

2. Gao, Z.; Mogni, L.V.; Miller, E.C.; Railsback, J.G.; Barnett, S.A. A perspective on low-temperature solid oxide fuel cells. *Energy Environ. Sci.* **2016**, *9*, 1602–1644. [CrossRef]

3. Adler, S.B. Factors governing oxygen reduction in solid oxide fuel cell cathodes. *Chem. Soc. Rev.* **2004**, *104*, 4791–4844. [CrossRef] [PubMed]

4. Murray, E.P.; Tsai, T.; Barnett, S.A. Oxygen transfer processes in (La,Sr)MnO$_3$/Y$_2$O$_3$-stabilized ZrO$_2$ cathodes: An impedance spectroscopy study. *Solid State Ion.* **1998**, *110*, 235–243. [CrossRef]

5. Minh, Q.; Takahashi, T. *Science and Technology of Ceramic Fuel Cell*; Elsevier: New York, NY, USA, 1995.

6. Painter, A.S.; Huang, Y.L.; Wachsman, E.D. Durability of $(La_{0.8}Sr_{0.2})_{0.95}MnO_{3-\delta}$-$(Er_{0.2}Bi_{0.8})_2O_3$ composite cathodes for low temperature SOFCs. *J. Power Sources* **2012**, *220*, 324–330. [CrossRef]

7. Marrero-López, D.; Dos Santos-Gómez, L.; Canales-Vázquez, J.; Martín, F.; Ramos-Barrado, J.R. Stability and performance of nanostructured $La_{0.8}Sr_{0.2}MnO_3$ cathodes deposited by spray-pyrolysis. *Electrochim. Acta* **2014**, *134*, 159–166. [CrossRef]

8. Pajot, M.; Duffort, V.; Capoen, E.; Mamede, A.-S.; Vannier, R.-N. Influence of the strontium content on the performance of $La_{1-x}Sr_xMnO_3/Bi_{1.5}Er_{0.5}O_3$ composite electrodes for low temperature Solid Oxide Fuel Cells. *J. Power Sources* **2020**, *450*, 227649. [CrossRef]

9. Backhaus-Ricoult, M. Interface chemistry in LSM–YSZ composite SOFC cathodes. *Solid State Ion.* **2006**, *177*, 2195–2200. [CrossRef]

10. Dos Santos-Gómez, L.; Zamudio-García, J.; Porras-Vázquez, J.M.; Losilla, E.R.; Marrero-López, D. Highly efficient $La_{0.8}Sr_{0.2}MnO_{3-\delta}$-$Ce_{0.9}Gd_{0.1}O_{1.95}$ nanocomposite cathodes for solid oxide fuel cells. *Ceram. Int.* **2018**, *44*, 4961–4966. [CrossRef]

11. Dos Santos-Gómez, L.; Losilla, E.R.; Martín, F.; Ramos-Barrado, J.R.; Marrero-López, D. Novel microstructural strategies to enhance the electrochemical performance of $La_{0.8}Sr_{0.2}MnO_{3-\delta}$ cathodes. *ACS Appl. Mater. Interfaces* **2015**, *7*, 7197–7205. [CrossRef]

12. Zapata-Ramírez, V.; Dos Santos-Gómez, L.; Mather, G.C.; Marrero-López, D.; Pérez-Coll, D. Enhanced Intermediate-Temperature Electrochemical Performance of Air Electrodes for Solid Oxide Cells with Spray-Pyrolyzed Active Layers. *ACS Appl. Mater. Interfaces* **2020**, *12*, 10571–10578. [CrossRef] [PubMed]

13. Li, W.; Guan, B.; Ma, L.; Tian, H.; Liu, X. Synergistic Coupling of Proton Conductors BaZr$_{0.1}$Ce$_{0.7}$Y$_{0.1}$Yb$_{0.1}$O$_{3-\delta}$ and La$_2$Ce$_2$O$_7$ to Create Chemical Stable, Interface Active Electrolyte for Steam Electrolysis Cells. *ACS Appl. Mater. Interfaces* **2019**, *11*, 18323–18330. [CrossRef] [PubMed]

14. Zhang, L.; Xia, C.; Zhao, F.; Chen, F. Thin film ceria–bismuth bilayer electrolytes for intermediate temperature solid oxide fuel cells with $La_{0.85}Sr_{0.15}MnO_{3-\delta}$–$Y_{0.25}Bi_{0.75}O_{1.5}$ cathodes. *Mater. Res. Bull.* **2010**, *45*, 603–608. [CrossRef]

15. Lee, K.T.; Jung, D.W.; Camaratta, M.A.; Yoon, H.S.; Ahn, J.S.; Wachsman, E.D. $Gd_{0.1}Ce_{0.9}O_{1.95}/Er_{0.4}Bi_{1.6}O_3$ bilayered electrolytes fabricated by a simple colloidal route using nano-sized $Er_{0.4}Bi_{1.6}O_3$ powders for high performance low temperature solid oxide fuel cells. *J. Power Sources* **2012**, *205*, 122–128. [CrossRef]

16. Leng, Y.J.; Chan, S.H. Anode-supported SOFCs with Y_2O_3-Doped Bi_2O_3/Gd_2O_3-Doped CeO_2 composite electrolyte film. *Electrochem. Solid State Lett.* **2006**, *9*, A56. [CrossRef]

17. Joh, D.W.; Park, J.H.; Kim, D.; Wachsman, E.D.; Lee, K.T. Functionally graded bismuth oxide/zirconia bilayer electrolytes for high-performance intermediate-temperature solid oxide fuel cells (IT-SOFCs). *ACS Appl. Mater. Interfaces* **2017**, *9*, 8443–8449. [CrossRef] [PubMed]

18. Hou, J.; Liu, F.; Gong, Z.; Wu, Y.; Liu, W. Different ceria-based materials $Gd_{0.1}Ce_{0.9}O_{2-\delta}$ and $Sm_{0.075}Nd_{0.075}Ce_{0.85}O_{2-\delta}$ for ceria–bismuth bilayer electrolyte high performance low temperature solid oxide fuel cells. *J. Power Sources* **2015**, *299*, 32–39. [CrossRef]

19. Hou, J.; Bi, L.; Qian, J.; Zhu, Z.; Zhang, J.; Liu, W. High performance ceria–bismuth bilayer electrolyte low temperature solid oxide fuel cells (LT-SOFCs) fabricated by combining co-pressing with drop-coating. *J. Mater. Chem. A* **2015**, *3*, 10219–10224. [CrossRef]

20. Ahn, J.S.; Camaratta, M.A.; Pergolesi, D.; Lee, K.T.; Yoon, H.; Lee, B.W.; Jung, D.W.; Traversa, E.; Wachsman, E.D. Development of High Performance Ceria/Bismuth Oxide Bilayered Electrolyte SOFCs for Lower Temperature Operation. *J. Electrochem. Soc.* **2010**, *157*, B376. [CrossRef]

21. Park, J.Y.; Yoon, H.; Wachsman, E.D. Fabrication and characterization of high-conductivity bilayer electrolytes for intermediate temperature solid oxide fuel cells. *J. Am. Ceram. Soc.* **2005**, *88*, 2402–2408. [CrossRef]

22. Zhang, L.; Li, L.; Zhao, F.; Chen, F.; Xia, C. $Sm_{0.2}Ce_{0.8}O_{1.9}/Y_{0.25}Bi_{0.75}O_{1.5}$ bilayered electrolytes for low-temperature SOFCs with $Ag-Y_{0.25}Bi_{0.75}O_{1.5}$ composite cathodes. *Solid State Ion.* **2011**, *192*, 557–560. [CrossRef]

23. Santos-Gómez, L.D.; Porras-Vázquez, J.M.; Losilla, E.R.; Marrero-López, D. Improving the efficiency of layered perovskite cathodes by microstructural optimization. *J. Mater. Chem. A* **2017**, *5*, 7896–7904. [CrossRef]

24. Dos Santos-Gómez, L.; Zamudio-García, J.; Porras-Vázquez, J.M.; Losilla, E.R.; Marrero-López, D. Highly oriented and fully dense CGO films prepared by spray-pyrolysis and different precursor salts. *J. Eur. Ceram. Soc.* **2020**, *40*, 3080–3088. [CrossRef]

25. *X'Pert HighScore Plus*; Malvern Panalytical: Almelo, The Netherlands, 2014.

26. *GSAS Program*; Rep. No. LA-UR-86748; Los Alamos, National Lab: Los Alamos, NM, USA, 1994.

27. Johnson, D. Z*View: A Software Program for IES Analysis*; Version 2.9; Scribner Associates, Inc.: Southern Pines, NC, USA, 2005.

28. Wan, T.H.; Saccoccio, M.; Chen, C.; Ciucci, F. Influence of the Discretization Methods on the Distribution of Relaxation Times Deconvolution: Implementing Radial Basis Functions with DRTtools. *Electrochim. Acta* **2015**, *184*, 483–499. [CrossRef]

29. Battle, P.D.; Catlow, C.R.A.; Heap, J.W.; Moroney, L.M. Structural and Dynamical Studies of δ-Bi_2O_3 Oxide Ion Conductors: I. The Structure of $(Bi_2O_3)_{1-x}(Y_2O_3)_x$ as a Function of x and Temperature. *J. Solid State Chem.* **1986**, *63*, 8–15. [CrossRef]

30. Gao, Z.; Zenou, V.Y.; Kennouche, D.; Marks, L.; Barnett, S.A. Solid oxide cells with zirconia/ceria Bi Layer electrolytes fabricated by reduced temperature firing. *J. Mater. Chem. A* **2015**, *3*, 9955–9964. [CrossRef]

31. Molin, S.; Chrzan, A.; Karczewki, J.; Szymczewska, D.; Jasinki, P. The role of thin functional layers in solid oxide fuel cells, Electrochim. *Acta* **2016**, *204*, 136–145. [CrossRef]

32. Pan, K.-J.; Hussain, A.M.; Huang, Y.-L.; Gong, Y.; Cohn, G.; Ding, D.; Wachsman, E.D. Evolution of Solid Oxide Fuel Cells via Fast Interfacial Oxygen Crossover. *ACS Appl. Energy Mater.* **2019**, *2*, 4069–4074. [CrossRef]

33. Fleig, J. Solid oxide fuel cell cathodes: Polarization mechanisms and modeling of the electrochemical performance. *Annu. Rev. Mater. Res.* **2003**, *33*, 361–382. [CrossRef]

34. Ghamarinia, M.; Babaei, A.; Zamani, C. Electrochemical characterization of La_2NiO_4-infiltrated $La_{0.6}Sr_{0.4}Co_{0.2}Fe_{0.8}O_{3-d}$ by analysis of distribution of relaxation times. *Electrochim. Acta* **2020**, *353*, 136520. [CrossRef]

35. Kromp, A.; Leonide, A.; Weber, A.; Ivers-Tiffée, E. Electrochemical Analysis of Reformate-Fuelled Anode Supported SOFC. *J. Electrochem. Soc.* **2011**, *158*, B980. [CrossRef]

36. Chen, Y.; Choi, Y.M.; Yoo, S.; Ding, Y.; Yan, R.; Pei, K.; Qu, C.; Zhang, L.; Chang, I.; Zhao, B.; et al. A highly efficient multi-phase catalyst dramatically enhances the rate of oxygen reduction. *Joule* **2018**, *2*, 938–949. [CrossRef]

37. Lee, J.G.; Park, M.G.; Yoon, H.H.; Soul, Y.G. Application of GDC-YDB Bilayer and LSMYDB Cathode for Intermediate Temperature Solid Oxide Fuel Cells. *J. Electroceram.* **2013**, *31*, 231–237. [CrossRef]

38. He, Z.; Ai, N.; He, S.; Jiang, S.P.; Zhang, L.; Rickard, W.D.A.; Tang, D.; Chen, K. Positive Effect of Incorporating $Er_{0.4}Bi_{1.6}O_3$ on the Performance and Stability of $La_2NiO_{4+\delta}$ Cathode. *J. Electrochem. Soc.* **2019**, *166*, F796–F804. [CrossRef]

39. Lenser, C.; Menzler, N.H. Impedance characterization of supported oxygen ion conducting electrolytes. *Solid State Ion.* **2019**, *334*, 70–81. [CrossRef]